Volume 11
Number 3
7 February 2021
Pages 691–1142

Catalysis Science & Technology

rsc.li/catalysis

ISSN 2044-4761

ROYAL SOCIETY OF CHEMISTRY

COMMUNICATION

Meenakshisundaram Sankar, Nora H. de Leeuw *et al.*
A surface oxidised Fe–S catalyst for the liquid phase hydrogenation of CO_2

Catalysis Science & Technology

ROYAL SOCIETY OF CHEMISTRY

COMMUNICATION

View Article Online
View Journal | View Issue

Cite this: *Catal. Sci. Technol.*, 2021, 11, 779

Received 11th September 2020,
Accepted 18th November 2020

DOI: 10.1039/d0cy01779e

rsc.li/catalysis

A surface oxidised Fe–S catalyst for the liquid phase hydrogenation of CO_2†

Claire E. Mitchell, [a] Umberto Terranova, [ab] Andrew M. Beale, [cd] Wilm Jones, [cd] David J. Morgan, [a] Meenakshisundaram Sankar *[a] and Nora H. de Leeuw *[ae]

Rapidly increasing anthropogenic carbon dioxide (CO_2) emissions, coupled with irreversible climate change and depleting fossil fuel reserves, have significantly increased the drive for CO_2 utilisation. Iron sulfide as a catalyst for the hydrogenation of CO_2 has been discussed in the literature for decades, especially in an origin-of-life context, but little experimental evidence exists in the literature for its feasibility. Here we report the catalytic properties of pyrrhotite ($Fe_{1-x}S$) for the hydrogenation of CO_2 into formate. Advanced material characterisation methods in combination with computational studies have allowed us to identify surface S–Fe–O moieties as active sites for the reaction.

Due to the high natural abundance, low cost and low toxicity of iron and sulfur, the last decade has seen attention focussed on iron sulfide structures, including pyrrhotite ($Fe_{1-x}S$), pyrite (FeS_2) and greigite (Fe_3S_4), for their potential in green catalytic applications and energy storage.[1–7] Fe–S phases have been hypothesised as potential membrane catalysts produced at hydrothermal vents, which reduce aqueous carbon dioxide (CO_2) in the formation of prebiotic molecules on the pathway to the emergence of life on early Earth,[8–10] owing to their unique similarities to iron and sulfur clusters within enzyme active sites. Following this lead, bio-inspired Fe–S catalysts such as FeS_2,[11] Fe_3S_4 (ref. 1) and $Fe_{4.5}Ni_{4.5}S_8$ (ref. 12 and 13) have been reported for the electrochemical reduction of CO_2. However, in these systems the reduction potential of the $H_2/2H^+$ couple is not sufficiently low to reduce CO_2 to formate ($HCOO^-$), formaldehyde (HCHO) or similar oxygenates,[14] resulting in poor activity and low product yields. Thermal catalysis in an alkaline medium, using high pressure CO_2, can overcome such challenges, and can be potentially used in large scale industrial production.

Herein, we present the catalytic properties of iron sulfide-based materials for the hydrogenation of CO_2 to formate under alkaline hydrothermal conditions, proceeding *via* a HCO_3^- intermediate. After pyrite, pyrrhotite is the most common and abundant iron sulfide mineral in nature and one of the most stable Fe–S phases, occurring as an accessory mineral in many rocks and found in a wide range of hydrothermal deposits.[15,16] Pyrrhotite is highly sensitive to oxygen and upon contact with air or moisture, the surface of the material spontaneously oxidises through an established process.[16–19] Our work focuses on investigating the effect of oxidation on the catalytic efficacy of these iron sulfide materials. By enhancing the catalytic properties of these materials, *via* controlled calcination, we report new possibilities for a cheap, non-toxic, readily available pyrrhotite-based catalyst.

Pyrrhotite materials were prepared using an adapted method reported by Beal *et al.*[20] (ESI†). The synthesis methodology uses rapid *in situ* sulfidization of the decomposition product of $Fe(acac)_2$ with elemental sulfur to form $Fe_{1-x}S$.[21–23] Pyrrhotite can be identified as the majority phase, as confirmed by XRD, Fig. 1a, presenting five major reflections at $2\theta \approx 31$, 34, 44, 53 and 71°, (JCPDS-PDF card no. 01-079-5974). Raman spectroscopy, Fig. 1b, showing bands at 215, 277 and 384 cm^{-1}, also perfectly correlate with reported Raman spectra of natural pyrrhotite.[24] The XRD patterns in Fig. S1† confirm the successful conversion of $Fe(acac)_2$ precursor to $Fe_{1-x}S$ without any iron carbide formation. Elemental analysis revealed an Fe : S ratio of 0.96 : 1, (Table S1†), which is consistent with the stoichiometry of hexagonal pyrrhotite.[25]

The lab-synthesised pyrrhotite was tested for the liquid phase CO_2 hydrogenation in an aqueous 1 M NaOH solution at 125 °C and at 20 bar pressure ($CO_2 : H_2$, 1 : 1 at 25 °C), see ESI† for full procedure. Previously, we have reported the hydrogenation of CO_2 using different alkaline solvents; NaOH, $NaHCO_3$ and Na_2CO_3[26] and found that NaOH is the

[a] *Cardiff Catalysis Institute, School of Chemistry, Cardiff University, Cardiff, CF10 4AT, UK. E-mail: sankar@cardiff.ac.uk*
[b] *School of Postgraduate Medicine and Allied Health, Crewe campus, University of Buckingham, Crewe, CW1 5DU, UK*
[c] *Department of Chemistry, University College London, London, WC1H 0AJ, UK*
[d] *Research Complex at Harwell, Rutherford Appleton Laboratory, Harwell Science & Innovation Campus, Harwell, Didcot, OX11 0FA, UK*
[e] *School of Chemistry, University of Leeds, Leeds, LS2 9JT, UK. E-mail: n.h.deleeuw@leeds.ac.uk*

† Electronic supplementary information (ESI) available. See DOI: 10.1039/d0cy01779e

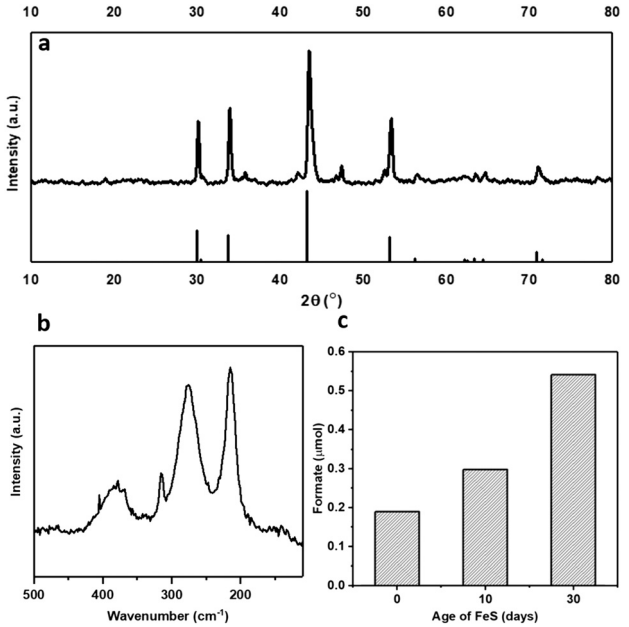

Fig. 1 Freshly synthesised pyrrhotite analysed by (a) XRD with pyrrhotite reference peaks (JCPDS 01-079-5974 PDF file) and (b) Raman spectroscopy. (c) Effect of aging the pyrrhotite catalyst in air on formate production.

most suitable base for this reaction. When NaOH was used, all the formate is produced from CO_2 rather than from the alkaline salt.[26] Based on these prior results, we have used NaOH in this study as well. After CO_2 dissolution, the pH of the reaction medium is *ca.* pH 6–8,[26] *i.e.* conditions favouring HCO_3^- species,[27] which is hence considered as the intermediate carbon species. Freshly synthesised pyrrhotite was found to be active for CO_2 hydrogenation, resulting in 0.19 μmols of formate after 3 days of reaction, Fig. 1c. Interestingly, pyrrhotite aged in air at room temperature and pressure for 30 days displayed a much better activity, yielding 0.54 μmols of formate under identical reaction conditions, stimulating a hypothesis that oxidation improves the activity of the material. To investigate this suggestion further, fresh pyrrhotite was calcined at different temperatures and tested for CO_2 hydrogenation, Fig. 2a. Calcination at 200 °C resulted in the most active catalyst, achieving the highest formate productivity of 1.00 μmol after 3 days, a significant improvement on the catalytic activity of pyrrhotite (0.29 μmol). However, increasing the calcination temperature above 200 °C resulted in reduced formate productivity (0.26 μmol for samples calcined at 250 °C). The first bar in Fig. 2a is the productivity of fresh sample kept at room temperature (25 °C) for several days, hence the formate productivity is higher than the fresh catalyst presented in Fig. 1c. XRD of a 200 °C calcined sample, Fig. 2b, revealed the presence of a poorly crystalline sample of lower symmetry, comprising a number of phases although their identification is ambiguous. A comparison with JCPDS database entries suggests the 200 °C pattern may comprise contributions from the original pyrrhotite, marcasite (FeS_2) (JCPS 01-074-1051 PDF file) and Fe_2O_3 (JCPS 01-085-0987 PDF

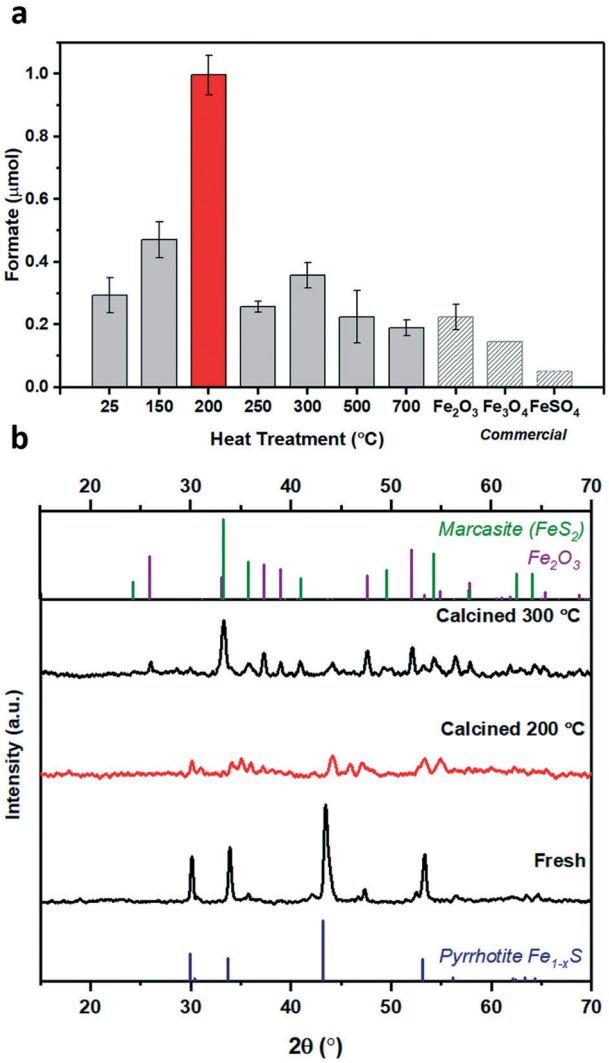

Fig. 2 (a) Comparison of the effect of different calcination temperatures pyrrhotite catalyst for the hydrogenation of CO_2 to produce formate, reaction conditions: catalyst: 20 mg; 1 M NaOH solution: 4 ml; $pCO_2:H_2$: (1 : 1) 20 bar; 125 °C for 3 days. (b) XRD spectra of pyrrhotite fresh, calcined at 200 °C, and calcined at 300 °C, compared to corresponding XRD patterns sourced PDF cards. (Blue) – pyrrhotite, 01-079-5974; (green) – marcasite, FeS_2, 01-074-1051; (purple) – Fe_2O_3, 01-085-0987.

file). However, an examination of the SEM before and after calcination (Fig. S2†) reveals no obvious formation of multiple phases (morphologies), but rather an overall reduction in particle size. The XRD pattern of a pyrrhotite sample calcined at 300 °C, Fig. 2b, shows evidence of the presence of marcasite and iron oxide, Fe_2O_3. The formation of these new Fe–S or Fe–O phases in correlation with loss in activity implies that they are not the source of the enhanced activity. Increasing the temperature beyond 300 °C leads to the formation of primarily Fe_2O_3, as determined by XRD in Fig. S3† and supported by TGA in Fig. S4,† which reveal a mass loss from 300 °C, implying Fe–S decomposition releasing SO_2. Commercial Fe_2O_3, Fe_3O_4 and $FeSO_4$ samples resulted in low formate productivity (Fig. 2a), thus eliminating the possibility of

their role as catalytic active site within our oxidised Fe–S catalyst. Heating pyrrhotite under an N_2 atmosphere at 200 °C also had little effect on the crystal structure of the pyrrhotite phase, and a reduced catalytic activity, most likely due to the absence of the surface oxide species (Fig. S5†). To understand the role of calcination on the structural properties of pyrrhotite and in turn its catalytic property, these materials were characterised by several spectroscopic and microscopic methods.

XPS spectra of a fresh pyrrhotite sample and a sample calcined at 200 °C are presented in Fig. 3a–d. The atomic surface ratio of Fe : S : O in a fresh pyrrhotite sample was 12 : 39 : 49, but in the calcined sample it was approximately 13 : 7 : 80. As pyrrhotite is highly air sensitive, exposure to oxygen forces Fe atoms to diffuse from the interior to the surface to combine with oxygen,[28] altering the surface Fe/S ratio. Calcination increased the rate of oxidation to form an oxygen-rich surface with an atomic percentage of 80%. TGA (Fig. S4†) revealed no significant mass loss at 200 °C, and therefore no sulfur had been removed from the surface as SO_2. Fe 2p analysis of fresh pyrrhotite surfaces, shown in Fig. 3a, reveals three distinct peaks at 710.1–713.3 eV, indicating the presence of oxidised iron. Another, smaller peak at 707.3 eV, indicates the presence of Fe(II)–S species.[28,29] Calcination of pyrrhotite increases the amount of surface Fe–O species and depletes surface Fe–S species (Fig. 3b), calculated from the atom concentrations listed in Table S1.† The S 2p spectrum (Fig. 3c and d) is fitted with a doublet representing the spin-orbit splitting of S $2p_{3/2}$ and S $2p_{1/2}$ lines. They show a dominance of monosulfide (S^{2-}) with peaks at 161.2 eV (2 $p_{3/2}$), but also disulfides (S_2^{2-}) with peaks at 162.2 eV (2 $p_{3/2}$), indicating the presence of S–Fe bonds. Also shown are polysulfides (S_n^{2-}) at 163.2 eV and elemental sulfur (164.1 eV). Finally, S $2p_{3/2}$ peaks are detected at binding energies of 166.6 and 168.2 eV, corresponding to SO_3^{2-} and SO_4^{2-} species, respectively. All mentioned binding energy values are similar to those reported by Pratt *et al.*[28] and Buckley *et al.*[29] Calcination at 200 °C, Fig. 3d, reveals an increase in SO_x species, whilst the monosulfides decrease in concentration with an increase in disulfides. The migration of Fe towards the surface to combine with oxygen, is evidenced by Fe–S (monosulfide) bond cleavage, leaving Fe vacancies within the structure and forcing the remaining Fe(II)–S to form disulfide bonds,[17,28] as evident in Table S2.† The formation of S–S bonds requires the oxidation of some sulfide (S^{2-}) to S^0, hence the increase in elemental sulfur.[28] These results suggest a surface of an oxide/hydroxide-rich layer with a small concentration of surface iron sulfide, and a sulfide-rich layer buried beneath the surface. As shown, calcining the catalyst from 200 °C to 300 °C causes a large drop in its activity. XPS reveals pyrrhotite calcined at 300 °C (Fig. S6†) has an atomic surface ratio of Fe : S : O at approximately 19 : 4 : 177, a dominantly iron oxide surface with a diminished sulfur content from 7% at 200 °C calcination to 4%. These results demonstrate that a significant amount of sulfur within an oxygen dominant surface is crucial for facilitating optimum catalytic activity. Hence, following our previous work with pyrrhotites,[30,31] density functional theory calculations have been employed to explore the role of sulfur atoms in the reduction of HCO_3^-, which is the dominant reactant species under the reaction conditions.

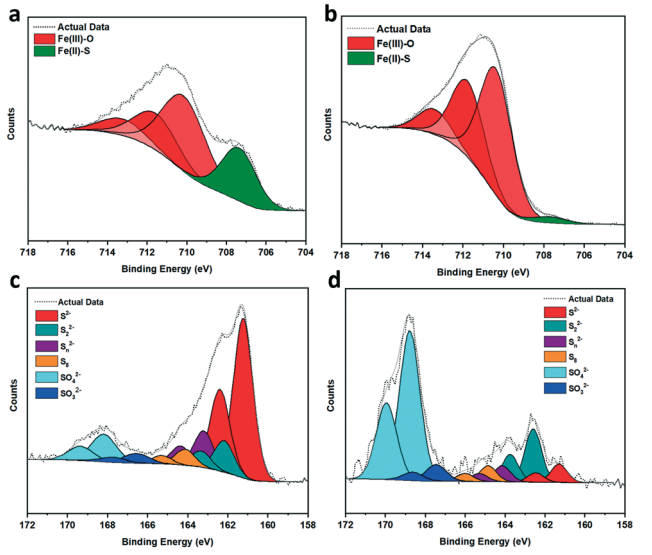

Fig. 3 (a–d) XPS spectra of fresh and calcined samples (a) Fe 2p, fresh (b) Fe 2p, calcined 200 °C (c) S 2p, fresh (d) S 2p, calcined 200 °C. Plot details in (Table S2†).

Previous computational investigation on a different iron sulfide – mixed-valence Fe_3S_4 greigite material – has reported that the aqueous phase reduction of HCO_3^- to $HCOO^-$ proceeds *via* the transfer of the OH^- species from a bridging adsorbate to the surface.[1] The remaining CO_2 molecule is activated to a bent geometry, which undergoes subsequent hydrogenation on the carbon atom. Similar to greigite, our findings have determined that the most stable adsorption of HCO_3^- on a fully oxidised pyrrhotite surface (termination A, Fig. S7a†) corresponds to a bridging vertical geometry, with an adsorption energy of −2.34 eV and Fe–O distances of 2.01 Å (Fig. 4a). However, we calculated that a considerable energy penalty of 2.08 eV was associated with the transfer of the OH group to the surface (Fig. S8†), which makes the greigite pathway thermodynamically unlikely, at least on the fully oxidised FeS (01−10) surface. Alternatively, the carbon atom can be attacked by a surface hydrogen, which reacts with the HCO_3^- hydroxyl group to eliminate a water molecule and the resulting CO_2 molecule can then be hydrogenated to $HCOO^-$. A similar pathway has been reported for the hydrogenation of HCO_3^- on nickel catalysts.[32] To investigate this pathway, we optimised the first $H_2CO_3^-$ intermediate, *i.e.* a structure where the carbon is hydrogenated and in a tetrahedral arrangement (Fig. 4b). The corresponding energy was 1.41 eV higher than the reactant configuration, while the high activation energy of 2.61 eV was again in line with the low efficiency of the fully oxidised surface. Interestingly, we found that the subsequent elimination of H_2O (Fig. S9†) is endothermic by only 0.39 eV, with a relatively low activation

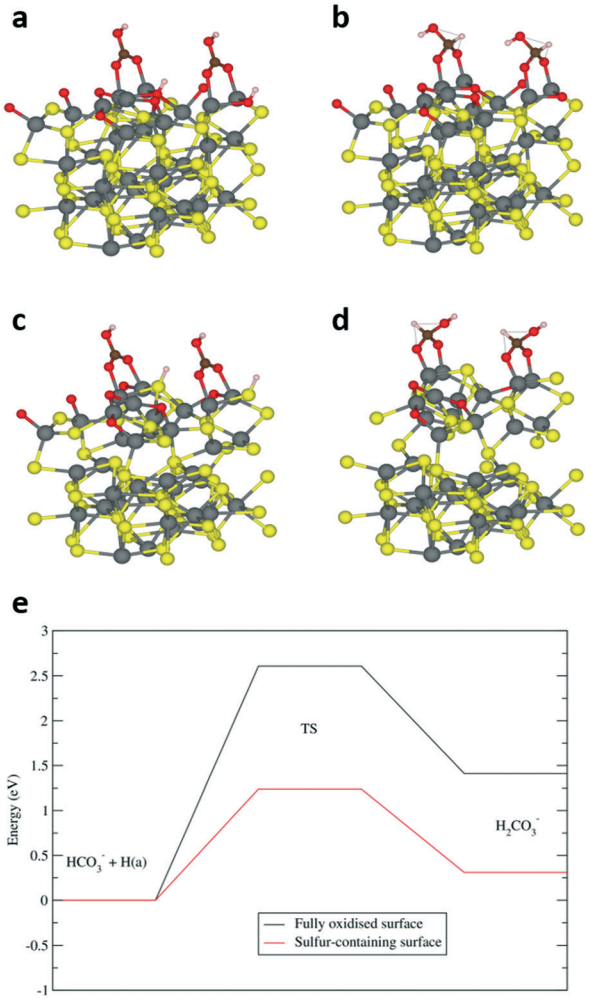

Fig. 4 Adsorption (a and c) and hydrogenation (b and d) structures of HCO_3^- on the fully oxidised termination A (a and b) and sulfur-containing termination B (c and d) of FeS stoichiometric pyrrhotite. Colour code: Fe-grey, S-yellow, O-red, C-brown, H-white. (e) Energetics of the carbon hydrogenation step on the fully oxidised termination A and sulfur-containing termination B surface showing the position of reactants (HCO_3^-), products ($H_2CO_3^-$) and transitions states (TS). The hydrogen species on the surface of the reactant configurations is indicated with H(a).

barrier of 1.25 eV which we would not expect to hinder the reaction, suggesting that the preceding carbon hydrogenation is the rate-limiting step.

A sulfur-containing surface (termination B, Fig. S7b†) leads to a very different scenario. The adsorption of HCO_3^-, with an energy of −1.75 eV, is still favoured, but the presence of the bulkier sulfur atom bends the adsorbate (Fig. 4c). In addition, the sulfur-bound hydrogen is closer to the carbon than the oxygen-bound hydrogen in termination A, which opens up the possibility of an alternative path for the hydrogen transfer leading to a tetrahedral carbon intermediate (Fig. 4d), which is only 0.31 eV higher in energy than the HCO_3^- reactant. Furthermore, its activation energy barrier of 1.24 eV is significantly reduced compared to the 2.61 eV reported above for termination A, which clearly highlights the importance of surface sulfur atoms in the HCO_3^- reduction process, as illustrated in the diagram of Fig. 4e.

To gain more understanding of the bulk structure, XAFS was employed. Data of fresh pyrrhotite, calcined at 200 °C and calcined at 300 °C, as well as a Fe_2O_3 reference are presented in Fig. 5a and b. XANES analysis provided the opportunity to study the oxidation state of the Fe K-edge (Fig. 5a). First to note is a very characteristic pre-edge (feature A) from the contribution of the Fe 1s → 3d transition.[33] There is a shoulder to the edge (B), indicating the coordination between Fe and S and representing the normally forbidden Fe 1s → 4s transition, which becomes more accessible, because the S 3p orbital overlap contributes p character to the Fe 4s orbital.[34] There is also white line intensity (C), corresponding to the first dipole-allowed Fe 1s → 4p transition.[35,36] Upon calcination at 200 °C, there is a shift towards lower energy of feature B, indicating that iron is oxidising upon calcination from Fe(II) to Fe(III), in particular losing Fe–S character and acquiring more O ligands. This finding is re-enforced by the Fourier transform EXAFS from a shift in radial distance at 2.2 Å, indicated in Fig. 5b. Calcination causes a small decrease in radial distance and a broader peak, indicating a mixture of Fe–S and Fe–O bonds. This effect is created owing to the fact that Fe(II) and S^{2-} are larger ions than Fe(III) and O^{2-}, therefore exhibiting a larger radial distance than Fe–O. Fe–S retains a bond distance in the range

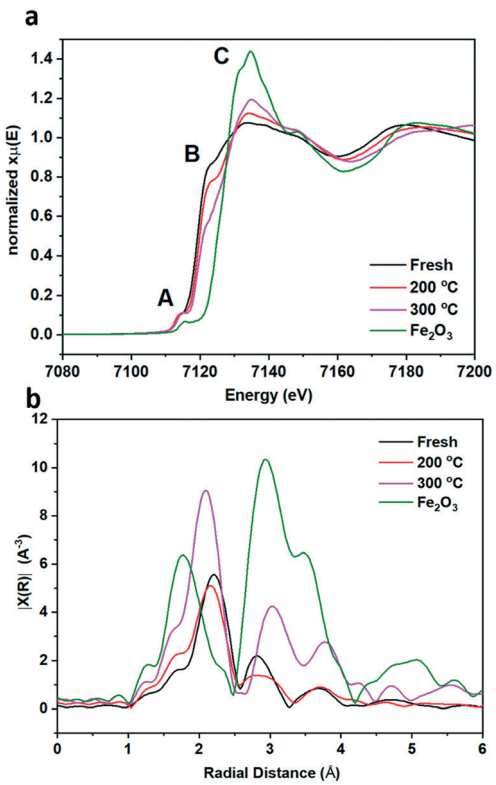

Fig. 5 XAS data of Fe K-edge including (a) XANES and (b) Fourier transform EXAFS for pyrrhotite samples; fresh (black), 200 °C calcination (red), 300 °C calcination (pink) and Fe_2O_3 reference sample (green). Blue arrows indicate direction of increasing oxygen ligands.

of 2.37–2.72 Å, whereas the Fe–O bond distance ranges from 1.81–1.93 Å. Our results show fresh pyrrhotite and Fe_2O_3 exhibit radial distances of 2.21 Å and 1.78 Å respectively, which are phase uncorrected results, hence the slight difference with actual Fe–O and Fe–S radial distances. The Fourier transform EXAFS reveals a particularly interesting feature: When the sample is calcined at 300 °C, a peak at ~2.8 Å starts to form. As this peak is also present in Fe_2O_3, it can be assigned as the Fe–Fe scattering component, consistent with the formation of bulk Fe_2O_3 from XRD. This peak is not present in the fresh and 200 °C calcined samples, showing that they do not contain iron oxide/iron hydroxide species. We have already confirmed that the 200 °C calcined sample shows that iron oxidation has occurred, whereas the shoulder edge B indicates Fe–S character, which together we suggest to be evidence for the formation of S–Fe–O species. Increasing the calcination temperature to 300 °C separates these species into separate Fe–O and Fe–S domains (as seen from the peak at ~2.8 Å). Since the formation of these Fe–O and Fe–S domains corresponds to a drop in the catalytic activity, S–Fe–O is a likely active species in this catalyst, corresponding well with the DFT calculations.

Conclusions

We have reported the synthesis of pyrrhotite ($Fe_{1-x}S$) and its catalytic activity towards the hydrogenation of CO_2 to formate under mild hydrothermal conditions, which is optimised by calcination. XPS and XAFS analysis has determined that oxidation of surface Fe–S species to form S–Fe–O species has a positive effect on the catalytic efficacy. Density functional theory calculations confirmed that the unique S–Fe–O interaction is critical in the carbon hydrogenation reaction, lowering the activation energy compared to the fully oxidised surface. The results from our preliminary investigation on the catalytic application of the Fe–S material, reported in this communication, is both exciting and promising. Further fine-tuning of this Fe–S material, inspired by the results presented here, has the potential to produce a more efficient, cheap and sustainable catalyst for CO_2 utilisation.

Conflicts of interest

There are no conflicts to declare.

Acknowledgements

The authors thank the Cardiff University scanning electron microscopy (SEM) and X-ray absorption spectroscopy (XPS) facilities, funded by EPRSC. We also thank the UK Catalysis Hub for allocating beamtime slots through the UK Catalysis Hub BAG allocation for X-ray acquisition of the transmission spectroscopic data at the Diamond synchrotron facility. This work was supported by the Engineering and Physical Sciences Research Council (grant EP/K009567/2) and used the ARCHER UK National Supercomputing Service (http://www.archer.ac.uk) *via* our membership of the UK's HEC Materials Chemistry Consortium, which is funded by EPSRC (EP/L000202). We acknowledge the support of the Supercomputing Wales project, which is part-funded by the European Regional Development Fund (ERDF) *via* Welsh Government. All data generated during this research are openly available from the Cardiff University Research Portal at http://doi.org/10.17035/d.2020.0098194792.

References

1 A. Roldan, N. Hollingsworth, A. Roffey, H.-U. Islam, J. B. M. Goodall, C. R. A. Catlow, J. A. Darr, W. Bras, G. Sankar, K. B. Holt, G. Hogarth and N. H. de Leeuw, *Chem. Commun.*, 2015, **51**, 7501–7504.
2 C. Di Giovanni, A. Reyes-Carmona, A. Coursier, S. Nowak, J. M. Greneche, H. Lecoq, L. Mouton, J. Roziere, D. Jones, J. Peron, M. Giraud and C. Tard, *ACS Catal.*, 2016, **6**, 2626–2631.
3 R. Miao, B. Dutta, S. Sahoo, J. He, W. Zhong, S. A. Cetegen, T. Jiang, S. P. Alpay and S. L. Suib, *J. Am. Chem. Soc.*, 2017, **139**, 13604–13607.
4 M. S. Faber, M. A. Lukowski, Q. Ding, N. S. Kaiser and S. Jin, *J. Phys. Chem. C*, 2014, **118**, 21347–21356.
5 D. Susac, L. Zhu, M. Teo, A. Sode, K. C. Wong, P. C. Wong, R. R. Parsons, D. Bizzotto, K. A. R. Mitchell and S. A. Campbell, *J. Phys. Chem. C*, 2007, **111**, 18715–18723.
6 H. Li, J. Liu, J. Li, Y. Hu, W. Wang, D. Yuan, Y. Wang, T. Yang, L. Li, H. Sun, S. Ren, X. Zhu, Q. Guo, X. Wen, Y. Li and B. Shen, *ACS Catal.*, 2017, **7**, 4805–4816.
7 T. A. Pecoraro and R. R. Chianelli, *J. Catal.*, 1981, **67**, 430–445.
8 G. Wächtershäuser, *Syst. Appl. Microbiol.*, 1988, **10**, 207–210.
9 M. J. Russell, R. M. Daniel, A. J. Hall and J. A. Sherringham, *J. Mol. Evol.*, 1994, **39**, 231–243.
10 V. Sojo, B. Herschy, A. Whicher, E. Camprubí and N. Lane, *Astrobiology*, 2016, **16**, 181–197.
11 M. G. Vladimirov, Y. F. Ryzhkov, V. A. Alekseev, V. A. Bogdanovskaya, V. A. Otroshchenko and M. S. Kritsky, *Origins Life Evol. Biospheres*, 2004, **34**, 347–360.
12 K. Pellumbi, M. Smialkowski, D. Siegmund and U. Apfel, *Chem. – Eur. J.*, 2020, chem.202001289.
13 S. Piontek, K. J. Puring, D. Siegmund, M. Smialkowski, I. Sinev, D. Tetzlaff, B. Roldan Cuenya and U.-P. Apfel, *Chem. Sci.*, 2019, **10**, 1075–1081.
14 N. Lane, *Cold Spring Harbor Perspect. Biol.*, 2014, **6**, a015982.
15 P. Toulmin III and P. B. Barton Jr, *Geochim. Cosmochim. Acta*, 1964, **28**, 641–671.
16 N. Belzile, Y.-W. Chen, M.-F. Cai and Y. Li, *J. Geochem. Explor.*, 2004, **84**, 65–76.
17 A. N. Buckley and R. Woods, *Appl. Surf. Sci.*, 1985, **22–23**, 280–287.
18 H. F. Steger and L. E. Desjardins, *Chem. Geol.*, 1978, **23**, 225–237.
19 M. P. Janzen, R. V. Nicholson and J. M. Scharer, *Geochim. Cosmochim. Acta*, 2000, **64**, 1511–1522.
20 J. H. L. Beal, P. G. Etchegoin and R. D. Tilley, *J. Solid State Chem.*, 2012, **189**, 57–62.

21 J. H. L. Beal, S. Prabakar, N. Gaston, G. B. Teh, P. G. Etchegoin, G. Williams and R. D. Tilley, *Chem. Mater.*, 2011, **23**, 2514–2517.
22 T. Li, H. Li, Z. Wu, H. Hao, J. Liu, T. Huang, H. Sun, J. Zhang, H. Zhang and Z. Guo, *Nanoscale*, 2015, **7**, 4171–4178.
23 A. Kirkeminde and S. Ren, *J. Mater. Chem. A*, 2013, **1**, 49–54.
24 Y. El Mendili, A. Abdelouas, H. El Hajj and J.-F. Bardeau, *RSC Adv.*, 2013, **3**, 26343.
25 F. Gronvold and H. Haraldsen, *Acta Chem. Scand.*, 1952, **6**, 1452–1469.
26 C. Mitchell, U. Terranova, I. AlShibane, D. J. Morgan, T. Davies, Q. He, J. Hargreaves, M. Sankar and N. H. De Leeuw, *New J. Chem.*, 2019, **43**, 13985–13997.
27 O. Pedersen, T. D. Colmer and K. Sand-Jensen, *Front. Plant Sci.*, 2013, **4**, 140.
28 A. R. Pratt, I. J. Muir and H. W. Nesbitt, *Geochim. Cosmochim. Acta*, 1994, **58**, 827–841.
29 A. N. Buckley and R. Woods, *Appl. Surf. Sci.*, 1985, **20**, 472–480.
30 U. Terranova and N. H. de Leeuw, *J. Phys. Chem. Solids*, 2017, **111**, 317–323.
31 U. Terranova, C. Mitchell, M. Sankar, D. Morgan and N. H. De Leeuw, *J. Phys. Chem. C*, 2018, **122**, 12810–12818.
32 C. S. He, L. Gong, J. Zhang, P. P. He and Y. Mu, *J. CO2 Util.*, 2017, **19**, 157–164.
33 M. Wilke, F. Farges, P. E. Petit, G. E. Brown and F. Martin, *Am. Mineral.*, 2001, **86**, 714–730.
34 M. Womes, R. C. Karnatak, J. M. Esteva, I. Lefebvre, G. Allan, J. Olivier-Fourcade and J. C. Jumas, *J. Phys. Chem. Solids*, 1997, **58**, 345–352.
35 S. N. A. Zakaria, N. Hollingsworth, H. U. Islam, A. Roffey, D. Santos-Carballal, A. Roldan, W. Bras, G. Sankar, G. Hogarth, K. B. Holt and N. H. De Leeuw, *ACS Appl. Mater. Interfaces*, 2018, **10**, 32078–32085.
36 Y. Mikhlin, Y. Tomashevich, S. Vorobyev, S. Saikova, A. Romanchenko and R. Félix, *Appl. Surf. Sci.*, 2016, **387**, 796–804.

